Strain perturbation method for atomic stress calculation with machine-learning potentials

Suyue Yuan,[1] Kwangnam Kim,[1] Bo Wang,[1] Wonseok Jeong,[2] Tae Wook Heo,[1]
Brandon C. Wood,[1] and Liwen F. Wan[1]

[1]*Laboratory for Energy Applications for the Future, Lawrence Livermore National Laboratory, Livermore, California 94550, USA*
[2]*Material Measurement Science Division, National Institute of Standards and Technology, Gaithersburg, Maryland 20899, USA*

(Received 20 September 2024; revised 31 January 2025; accepted 21 July 2025; published 7 August 2025)

Accurate computation of local atomic virial stress is crucial for predicting materials' mechanical response in large-scale molecular dynamic simulations, but conventional methods struggle with high-order atomic environment descriptors' encoded machine-learning many-body potentials. Herein we propose the strain perturbation method, a general framework that can efficiently compute high-resolution atomic virial stress. While remaining consistent with pairwise virial formulation, this method is broadly applicable and robust across many-body potentials with various atomic environment descriptors.

DOI: 10.1103/jg6w-fdl8

I. INTRODUCTION

In atomistic simulations, the concept of "atomic virial stress" is broadly used to probe local mechanical and thermal response of materials. It is particularly useful for describing physical processes such as defect nucleation, phase transformation, shock loading, and film growth [1–6], where local stress and strain distributions are highly heterogeneous due to material imperfections like vacancies, dislocations, and grain boundaries [7–10]. Accurate predictions of local stress distributions at the atomic scale are essential for assessing the microscopic state of materials and correlating their thermomechanical stability with processing and operational conditions. Among various formulations for deriving local stress tensors in molecular dynamics (MD) simulations [11–13], instantaneous atomic virial stress representation remains a favored choice given its flexibility to be seamlessly integrated into the main computation loop of MD simulations, which solely relies on collections of atomic coordinates, velocities, and pairwise forces [14–19].

However, the ongoing paradigm shift in MD simulations—from using classical interatomic potentials with explicit bond descriptions to machine-learning (ML) potentials with high-order local atomic environment descriptors—poses new challenges for atomic virial calculations. Conventional approaches to address many-body interactions, such as the group method [18], suffer from diminished spatial resolution due to their averaging scheme with inclusion of large atomic clusters using a single local environment descriptor. This limitation practically prevents deconvolution of elementwise contributions to atomic virials in multielement systems. Alternatively, force decomposition schemes [20], such as the covariant central force decomposition (cCFD) method [21,22], are computationally expensive and prone to uncertainties raised from specific force partitioning algorithms used in ML potentials. To address these challenges faced by the conventional methods of computing the atomic virial stress, we introduce a strain perturbation (SP) method as a general framework for extracting high-resolution atomic virial stress tensors with low computational cost. This method is broadly applicable and robust to pairwise and many-body potentials, ranging from classical to ML-based formalisms, and is particularly effective in handling intricate high-order atomic environment descriptors that will continue to emerge in future force-field architectures.

II. CHALLENGES OF ATOMIC STRESS CALCULATION FOR ML POTENTIALS

The main challenge in extracting atomic virials from ML potentials lies in their high-order local environment descriptors encoding complex many-body interactions. These descriptors can take different forms. For instance, in the spectral neighbor analysis potential (SNAP), the atomic local environment is described by a set of bispectrum components of the local neighbor density projected onto a basis of hyperspherical harmonics in four dimensions [23]. In the high-dimensional neural network potential (HDNNP), the local environment information is encoded with a set of symmetry functions, which then serve as inputs to atomic neural networks (ANNs) [24–26]. Given the growing interest in using the HDNNP in materials simulations, we consider it as a representative example to illustrate the limitations of conventional atomic virial calculation methods (original formulations are detailed in Supplemental Material S1 [27]) when encountering high-order local environment descriptors.

In HDNNPs, the total system energy is computed as the sum of atomic contributions, $U = \sum_i E_i$. Many-body forces arise from nonlinear activations in the hidden layers of ANNs. Therefore, special attention is required when deriving atomic stress, as the subforces are not pairwise. The total force on each atom is given by

$$\boldsymbol{F}_i = \sum_{I_\Omega : I_\Omega \in \Omega} \boldsymbol{F}_i^{I_\Omega} = -\sum_{I_\Omega : I_\Omega \in \Omega} \frac{\partial E_{I_\Omega}}{\partial \boldsymbol{R}_i} = -\sum_{j : j \in \Omega} \sum_{m_j=1}^{M_j} \frac{\partial E_j}{\partial G_j^{m_j}} \frac{\partial G_j^{m_j}}{\partial \boldsymbol{R}_i}, \tag{1}$$

where $\boldsymbol{F}_i^{I_\Omega}$ denotes the subforce contributed by the atom cluster I_Ω, $\boldsymbol{R}_i$ denotes the coordinates of atom i, $G_j^{m_j}$ are symmetry functions (see their typical expressions in Appendix 1) describing atom j, and $E_j \equiv E_{I_\Omega}$ is the atomic energy of atom j determined by atom cluster I_Ω. The set Ω comprises all neighbors within the cutoff radius of atom i, as well as those for which atom i lies within their own cutoff. Consequently, $\boldsymbol{F}_i$ depends not only on its direct neighbors (pink region in Fig. 5) but also on atoms within neighbors' cutoffs (blue and yellow regions).

Substituting $\boldsymbol{F}_i^{I_\Omega}$ into the group-based atomic stress formalism [23] and distributing the virial term equally among atoms within the group [28,29] yields

$$\boldsymbol{\pi}_i^{\text{HDNNP, group}} = -\frac{1}{\Omega_i}\left(\sum_{I_\Omega : I_\Omega \in \Omega} \frac{1}{N_{I_\Omega}} \sum_{j \in I_\Omega} \boldsymbol{R}_j^{I_\Omega} \otimes \boldsymbol{F}_j^{I_\Omega}\right), \quad (2)$$

where $\boldsymbol{\pi}_i$ is the atomic virial stress of atom i, Ω_i is its atomic volume, and N_{I_Ω} is the number of atoms in each cluster I_Ω (i.e., group). This formulation possesses a spatial-averaging nature: as I_Ω encompasses more atoms, atomic-scale stress resolution is compromised, making it challenging to resolve elementwise contributions in multielement systems. In practice, HDNNPs typically employ a cutoff radius of 6–10 Å to account for short-to-medium-range interactions [26]. Such a large cutoff radius can result in each atomic cluster containing hundreds of atoms, drastically reducing the spatial resolution of obtained atomic stress compared to classical many-body potentials, where each group generally consists of only a few atoms.

Alternatively, applying the cCFD method [21,22] requires decomposing each subforce $\boldsymbol{F}_i^{I_\Omega}$ into pairwise terms on the shape space $\mathcal{S}_{I_\Omega}$:

$$\boldsymbol{F}_i^{I_\Omega} = \sum_{j : j \in I_\Omega} \boldsymbol{F}_{ij}^{I_\Omega} = \sum_{j : j \in I_\Omega} \left[\left(\nabla_{\mathcal{S}_{I_\Omega}} \tilde{E}_{I_\Omega}\right)_{ij} \hat{\boldsymbol{R}}_{ij}\right], \quad (3)$$

where $\mathcal{S}_{I_\Omega}$ is defined by all distances $\|\mathbf{x}_j - \mathbf{x}_i\|$ among K atoms within I_Ω. Then the atomic stress can take a pairwise form:

$$\boldsymbol{\pi}_i^{\text{HDNNP,cCFD}} = -\frac{1}{2\Omega_i}\left(\sum_{I_\Omega : I_\Omega \in \Omega} \sum_{j : j \in I_\Omega} \boldsymbol{F}_{ij}^{I_\Omega} \otimes \boldsymbol{R}_{ij}^{I_\Omega}\right). \quad (4)$$

While Eq. (4) resolves the resolution issue of the group method [Eq. (2)], it incurs high computational cost. Solving Eq. (3) involves a QR decomposition on an $m \times n$ matrix with time complexity of $\mathcal{O}(mn^2)$ [22]. For a K-body system, $m = (K-1)K/2$ and $n = 3K$. This translates to $\mathcal{O}(K^4)$ per subforce decomposition.

More problematically, both the group and cCFD methods rely on subforce information, $\boldsymbol{F}_i^{I_\Omega}$. However, these subforces are intermediate outputs of the ML architecture and are not explicitly benchmarked during the training process of ML potentials. Only the total force $\boldsymbol{F}_i$ and atomic energy E_i (and occasionally the global virial stress) are trained and validated against the *ab initio* data. This raises concerns about the accuracy of deriving atomic virials directly from these subforces, as they are determined by a specific force partitioning scheme used in ML architecture. Since this partitioning can be nonunique and purely mathematical, unphysical artifacts like self-forces may arise.

III. STRAIN PERTURBATION METHOD FOR ATOMIC STRESS CALCULATION

As discussed above, conventional atomic stress calculation methods encounter challenges when dealing with local atomic environment descriptors employed in ML many-body potentials. To address issues related to spatial resolution, computational cost, and subforce accuracy, here we propose the SP method, broadly applicable to classical and ML-based many-body potentials. The SP method relies on two requirements: (1) the total energy of the system can be described additively as contributions from each atom, $U := \sum_i E_i$, and (2) each atomic potential function $E_i(\{\boldsymbol{r}_i\})$ is continuously differentiable and invariant under Euclidean transformations, hence allowing it to be mapped to the shape space, $\mathbb{R}^{3N} \to S : (\boldsymbol{x}_1, \cdots, \boldsymbol{x}_N) \mapsto (r_{12}, \cdots, r_{(N-1)N})$, i.e., $E_i(\{\boldsymbol{r}_i\}) := \widetilde{E}_i(\{r_{ij}\})$ [20]. Next, treating each atom as an individual system, we write its static part of stress tensor $\pi_i^{\alpha\beta}$ as the derivative of its strain energy:

$$\pi_i^{\alpha\beta} = \frac{1}{\Omega_i}\frac{\partial E_i(\{\boldsymbol{r}_i\})}{\partial \epsilon_i^{\alpha\beta}} = \frac{1}{\Omega_i}\frac{\partial \widetilde{E}_i(\{r_{ij}\})}{\partial \epsilon_i^{\alpha\beta}}, \quad (5)$$

where Ω_i is the atomic volume and $\epsilon_i^{\alpha\beta}$ is the strain component imposed on atom i (α, β being x, y, or z). We show in Appendix 2 that Eq. (5) is equivalent to the virial stress expressed in pairwise form when E_i is a pairwise potential. In its finite-difference form,

$$\pi_i^{\alpha\beta} = \frac{1}{\Omega_i}\frac{\Delta E_i(\{r_{ij}\})}{\Delta \epsilon_i^{\alpha\beta}}, \quad (6)$$

where ΔE_i is the energy change of atom i under an additional infinitesimal strain $\Delta\epsilon_i^{\alpha\beta}$. Consider an additional infinitesimal strain field introduced to the atomic system through uniform deformation of the simulation box. The strain field is defined as $\Delta\epsilon := \frac{1}{2}(\nabla_{\mathbf{R}}\mathbf{u} + (\nabla_{\mathbf{R}}\mathbf{u})^{\mathrm{T}})$, where $\nabla_{\mathbf{R}}\mathbf{u}$ is the displacement gradient tensor. Under this strain field, all pairwise distance vectors are transformed from $\boldsymbol{r}_{ij}$ to $\boldsymbol{r}_{ij}'$ via the relation $\boldsymbol{r}_{ij}' = (\mathbf{I} + \nabla_{\mathbf{R}}\mathbf{u}) \cdot \boldsymbol{r}_{ij}$. Accordingly, the strain experienced by each pairwise distance vector in the set $\{r_{ij}\}$, denoted as $\Delta\epsilon_{ij}^{\alpha\beta}$, is equivalent to the global strain imposed on the simulation box, i.e., $\Delta\epsilon_{ij}^{\alpha\beta} = \Delta\epsilon^{\alpha\beta}$. If we consider the strain imposed on atom i identical to the strain on the set of pairwise distances $\{r_{ij}\}$ that define its geometric space and contribute to its atomic energy, i.e., $\Delta\epsilon_i^{\alpha\beta} = \Delta\epsilon_{ij}^{\alpha\beta} = \Delta\epsilon^{\alpha\beta}$, then

$$\pi_i^{\alpha\beta} = \frac{1}{\Omega_i}\frac{\Delta E_i}{\Delta \epsilon^{\alpha\beta}}. \quad (7)$$

Remarkably, Eq. (7) preserves atomic-scale resolution without requiring any knowledge of subforces, thus overcoming the limitations of the group and cCFD methods described by Eqs. (2) and (4). Furthermore, a volume partition strategy [16,30] can be applied to Eq. (7):

$$\pi^{\alpha\beta}(\boldsymbol{R}) = \sum_{i \in \Omega_C} \frac{1}{\Omega_C}\frac{\Delta E_i}{\Delta \epsilon^{\alpha\beta}}, \quad (8)$$

where $\pi^{\alpha\beta}(\boldsymbol{R})$ is the static atomic stress centered at position $\boldsymbol{R}$, and Ω_C is the local volume defined by a customized cutoff criterion. When Ω_C includes all atoms in the system, Eq. (8) recovers the static part of global stress derived from the thermodynamic pressure (see derivations in Appendix 3).

Since the SP method relies on second-order derivatives of atomic energy, its accuracy is sensitive to the magnitude of the applied perturbation strain and continuity of the interatomic potential. Benchmark tests are necessary to determine the optimal perturbation value for each system, although a range of 10^{-4} to 10^{-2} is generally recommended. Additionally, the choice of a central difference scheme—combining tensile (positive) and compressive (negative) perturbations—should depend on the characteristics of the interatomic potential. For systems with hard-core interactions, compressive perturbations shall be used exclusively. Further details on implementation of the SP method are provided in Supplemental Material S2 [27].

IV. RESULTS AND DISCUSSION

We now benchmark the performance of the SP method across various classical and ML-based potentials. Details of the MD simulations using LAMMPS [31] and relevant calculation results are provided in Supplemental Material S3 [27]. Since volume partitioning for Ω_i is not the focus of this work and can be handled consistently (e.g., via Voronoi tessellation [32]), here we directly compare the instantaneous atomic virials, $\boldsymbol{w}_i = \Omega_i \cdot \boldsymbol{\pi}_i$, obtained from different atomic stress calculation methods. We first validate the SP method using a classical pairwise potential, where a rigorous solution based on pairwise forces exists, i.e., Eq. (A3) in Appendix 2. Figure 1(a) shows snapshots of the instantaneous atomic virial tensor components calculated for a pseudo-two-dimensional copper sample with randomly induced vacancy defects in its pristine face-centered-cubic structure, simulated using a Morse potential [33]. As expected, the atomic virials computed via the SP method align precisely with those calculated from the strict pairwise formulation. Parity plots for all six atomic virial components, evaluated using a perturbation strain of 10^{-3}, as shown in Fig. 1(b), further confirm the consistency of the SP method with pairwise virial definition. Additional results for different perturbation strains and equilibrium stages are provided in Supplemental Material Figs. S3–S5 [27]. There results demonstrate the robustness of the SP method across a broad range of perturbation strains (10^{-3} to 10^{-2}) and throughout transitions from far-from-equilibrium to quasiequilibrium states during the MD simulations.

We next benchmark the performance of the SP method against the group method using a classical three-body potential. This scenario represents a case where the group method is generally reliable, as each group involves only three atoms, alleviating the spatial resolution issues. Figures 2(a)–2(c) present snapshots of a silicon sample with vacancy defects in its diamond-cubic structure under a 2% compressive strain in the y direction, simulated using the Stillinger-Weber potential [35]. Overall, the atomic virials obtained from the SP and group methods show good agreement. However, noticeable differences appear near the defect sites. The atomic virials calculated via the SP method exhibit a twofold rotational symmetry about the z axis [Fig. 2(c)], reflecting the intrinsic symmetry of the defected material. In contrast, this symmetry is absent in the group method results, likely due to distortions in the geometric center of interacting atoms within each group. Interestingly, the same rotational symmetry is confirmed in later simulations using an ML potential (Fig. 3), suggesting that the SP method yields more consistent results across different interatomic potentials.

To highlight the capability of the SP method in resolving high-resolution atomic virials under scenarios where each group encompasses a large atomic cluster, the modified embedded atom model (MEAM) potential is considered for demonstration. In MEAM, many-body interactions arise from an embedded energy term that accounts for electron density contributions to the system energy, effectively serving as a simple local atomic environment descriptor that includes all atoms within the cutoff radius. As shown in Figs. 2(d)–2(f), we simulate a copper sample using a MEAM potential [36] under conditions similar to those in Fig. 1. While the group and SP methods yield comparable atomic virials in regions away from defects, notable differences appear near the defect sites. The w_{xx} values obtained from the SP method exhibit greater spatial variation, whereas those from the group method appear smoother. This disparity results from the group method's "averaging" nature, which is amplified when large atomic clusters are treated as single groups. To confirm that resolution is the primary factor behind these differences, we apply spatial averaging to the SP results: $\boldsymbol{w}_i^{\text{avg}} = \frac{1}{N_i}\sum_{j\in\Omega_i}\boldsymbol{w}_j$, where Ω_i is a spherical region centered at atom i, defined by the cutoff radius of the interatomic forces (4 Å), and N_i is the total number of atoms within Ω_i. As shown in Fig. 2(f), the spatially averaged SP results yield good agreement with the group method results. This comparison underscores the robustness of obtaining high-resolution atomic virials from the SP method and demonstrates the SP method's ability to reproduce smoothed virial distributions if necessary.

Having established the robustness of the SP method for various classical potentials, we now extend our analysis to ML-based many-body potentials with more complex high-order local atomic descriptors. As a first example, we simulate a silicon sample under conditions similar to those in Fig. 2(a), using a SNAP potential [23]. In the SNAP framework, local atomic environments are encoded as bispectrum components, making each subforce on an atom dependent on the coordinates of all atoms within the cutoff radius. As expected, the spatial resolution of atomic virials derived from the group method is diminished, as evidenced in Figs. 3(a)–3(c). In contrast, the SP method resolves finer spatial variations in the derived atomic virial components, revealing that the strongest tensile and compressive contributions emerge from the third to fifth nearest neighbors around the defects [Figs. 3(d)–3(f)]. To verify consistency between the results from these two methods, we apply spatial averaging to the SP results using the same 4.87-Å cutoff radius prescribed by the SNAP functionals. As shown in Figs. 3(g)–3(i), the spatial-averaged SP method reproduces the group method results, highlighting both the robustness and flexibility of the SP method when applied to ML-based potentials, regardless of the explicit formalism of their local atomic descriptors.

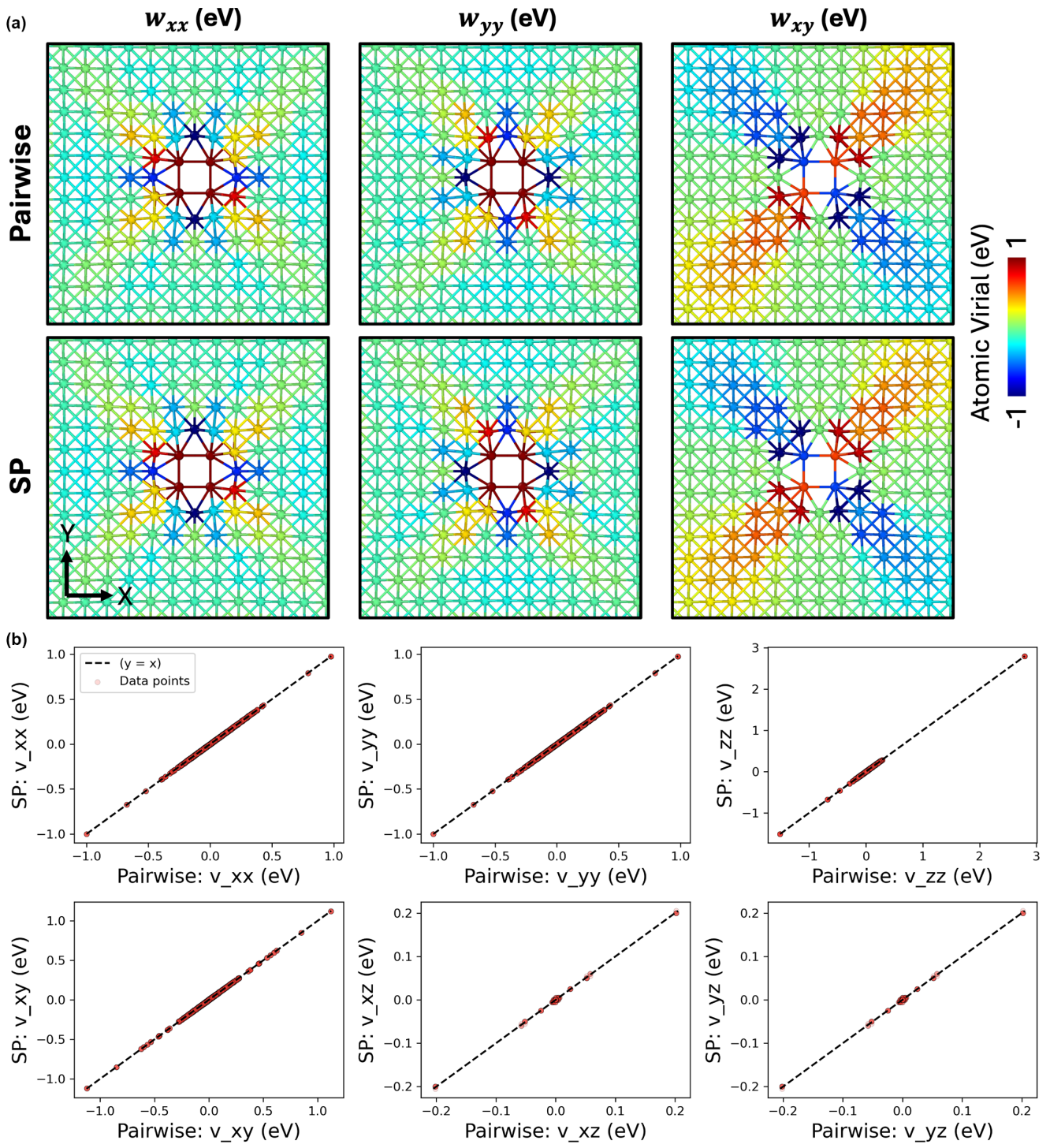

FIG. 1. Local atomic virial distributions in a copper sample with random vacancy defects, simulated using a pairwise Morse potential. (a) Spatial distribution of atomic virials calculated using the strict pairwise formulation (top row) and the strain perturbation (SP) method (bottom row), visualized by OVITO [34]. (b) Parity plots comparing all six atomic virial components obtained from the pairwise formulation and the SP method.

As a second example, we benchmark the SP method for a multielement system to demonstrate its capability in resolving elementwise contributions to atomic virials. Specifically, we conduct simulations on a garnet-type solid electrolyte $Li_7La_3Zr_2O_{12}$ (LLZO) using an HDNNP [37]. The LLZO sample contains a central crack and is subjected to mode-I fracture under external hydrostatic tension. As discussed earlier, the local atomic environment in HDNNPs is encoded with symmetry functions and the ANNs are tailored to each chemical component. Figures 4(a) and 4(d) depict the atomic virials incorporating contributions from all chemical species, calculated using the group method and the spatial-averaged SP method, respectively. While both methods yield broadly similar virial distributions, the group method displays more

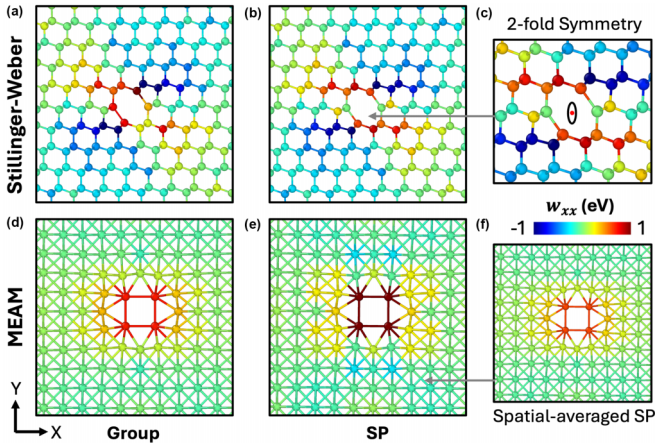

FIG. 2. Local atomic virial distributions in materials with vacancy defects. (a)–(c) Silicon simulated with a Stillinger-Weber potential. (d)–(f) Copper simulated with a MEAM potential. (a), (d) Results from the group method. (b), (e) Results from the SP method. (c) Zoom-in view of (b). (f) Spatially averaged version of (e).

pronounced atomic-scale fluctuations. These fluctuations can likely be attributed to the inherent force-partitioning scheme used in the HDNNP framework.

Next, we examine the local atomic virials of specific chemical sublattices. Within the group method formulation, atomic virials are not element specific owing to their aggregation across all species in the group. As a result, when displaying only atoms of specified types, such as the Zr-O sublattice

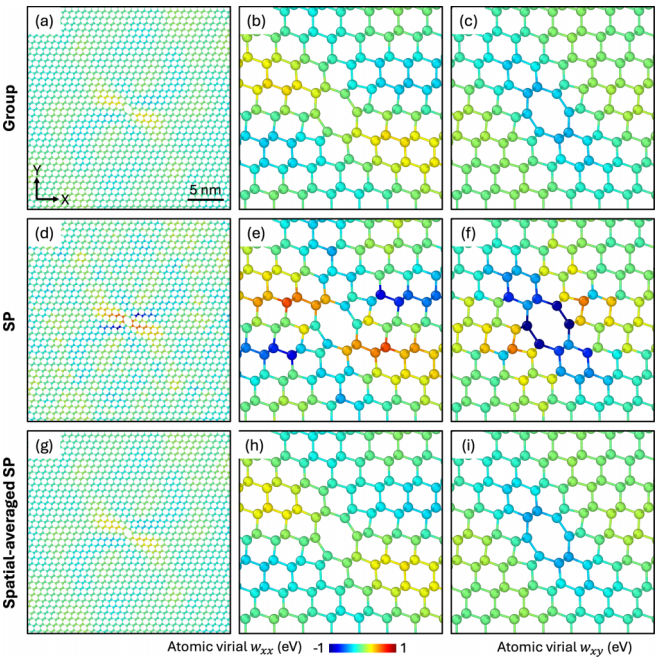

FIG. 3. Local atomic viral distributions in silicon with vacancy defects, simulated using the SNAP. (a)–(c) Results from the group method. (d)–(f) Results from the SP method. (e), (f) Results from the spatial-averaged SP methods. The left, middle, and right columns correspond to the zoom-out views of $\boldsymbol{w}_{xx}$, zoom-in views of $\boldsymbol{w}_{xx}$, and zoom-in views of $\boldsymbol{w}_{xy}$, respectively.

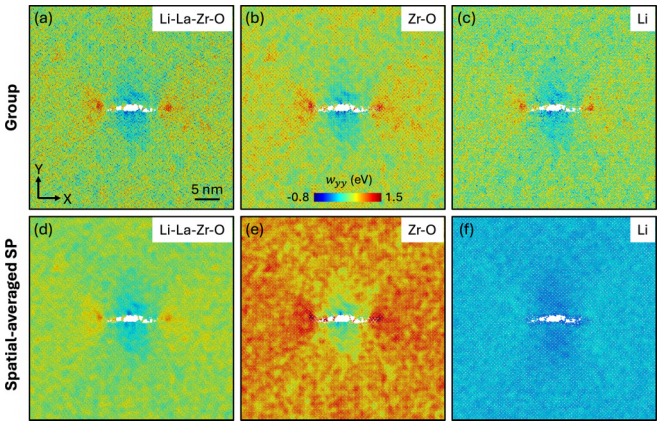

FIG. 4. Local atomic viral $\boldsymbol{w}_{yy}$ distributions in a $Li_7La_3Zr_2O_{12}$ (LLZO) with a center crack simulated with the HDNNP. (a)–(c) Results from the group method. (d)–(f) Results from the spatial-averaged SP method. The left, middle, and right columns correspond to the atomic virials extracted from the whole system, Zr-O sublattice, and Li ion sublattice, respectively.

in Fig. 4(b) and the Li sublattice in Fig. 4(c), their local atomic virial profiles closely resemble the overall distributions in Fig. 4(a). In contrast, the SP method allows spatial averaging to be performed exclusively on atoms of specified types, expressed as $\boldsymbol{w}_i^{\mu,\mathrm{avg}} = \frac{1}{N_i}\sum_{j\in\Omega_i}\boldsymbol{w}_j^{\mu}$, $\mu \in M$, where the superscript μ denotes the atom type, M represents the sublattice (i.e., the set of element types) of interest, and N_i is the number of atoms of the specified type within the cutoff region Ω_i. When applying the spatial-averaged SP method to a given sublattice and only displaying it, significant distinctions are revealed: the Zr-O sublattice withstands most of the tensile stress, with prominent stress concentration at the crack tip [Fig. 4(e)]. In contrast, Li ions primarily experience mild compressive stress, with only minor variations near the crack tip [Fig. 4(f)]. This observation aligns with the structural characteristics of LLZO, where Zr^{4+} ions form strong ionic bonds with O^{2-} in an octahedral configuration, featuring a rigid backbone in the LLZO structure that bears most of the mechanical strength. By comparison, Li ions reside in interstitial or vacancy sites within the Zr-O and La-O framework, where their weak interactions with the surrounding lattice minimize their subjection to the loaded tensile stress. As a result, local stress is largely concentrated on the Zr-O sublattice, while Li ions remain relatively unaffected during mechanical deformation. This example underscores the practical advantage of the SP method in resolving elementwise contributions to atomic virials/stresses, which is crucial for the understanding of chemomechanical coupling effects in solid-state batteries.

Beyond the above benchmark tests evaluated using atomic virials, we provide additional local virial stress results in Supplemental Material S4 [27], to showcase the effectiveness of the SP method in both equilibrium and nonequilibrium MD simulations.

V. CONCLUSIONS

We discussed the challenges of using conventional approaches to evaluate atomic virial stress in material systems

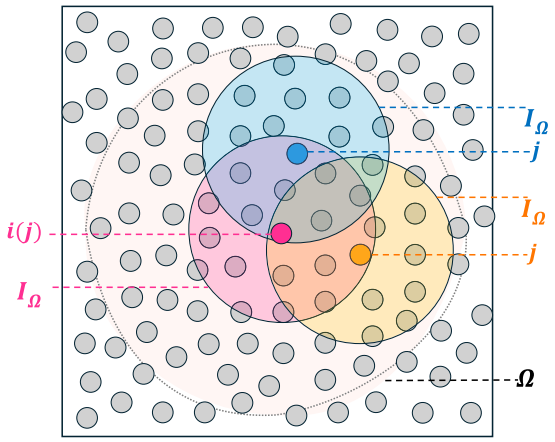

FIG. 5. Illustration of the spatial relationships between indices i, j, I_Ω, and Ω in a high-dimensional neural network configuration.

modeled with many-body ML potentials. To address these challenges, we introduce a strain perturbation method as a general framework capable of extracting high-resolution atomic virial stress tensors with low computational cost. The SP method is derived from a mechanical framework and features a mathematical formulation consistent with the rigid pairwise formulation for pairwise potentials while remaining applicable to complex many-body interactions. We demonstrate that the SP method is computationally more efficient than the cCFD method and can provide higher resolution and consistent results than the group method across various classical and ML-based potentials. The SP method is particularly well suited for handling intricate, high-order atomic environment descriptors, making it a flexible approach for deriving atomic virial stress in future generations of complex ML-potential architectures.

ACKNOWLEDGMENTS

This work was sponsored by the Office of Energy Efficiency and Renewable Energy, Vehicle Technologies Office and was performed under the auspices of the U.S. Department of Energy by Lawrence Livermore National Laboratory under Contract No. DE-AC52-07NA27344. Computing support for this work came from the Department of Energy's Office of Energy Efficiency and Renewable Energy located at the National Renewable Energy Laboratory and the Computing Grand Challenge program from Lawrence Livermore National Laboratory.

DATA AVAILABILITY

The workflows, scripts, and datasets used in this study are available in the public repository at [38]. Additional data supporting the findings are available from the authors upon reasonable request.

APPENDIX

1. Symmetry functions for HDNNPs

Symmetry functions usually include radial and angular types [25]. A typical radial symmetry function is expressed using Gaussian functions:

$$G_i^{\mathrm{rad}} = \sum_{j\neq i} e^{-\eta\left(R_{ij}-R_s\right)^2} f_c(R_{ij}), \tag{A1}$$

where R_{ij} is the distance between atom i and j, and $f_c(R_{ij})$ is the cutoff function. A typical angular symmetry function uses cosine functions to capture bond angle information:

$$G_i^{\mathrm{ang}} = 2^{1-\zeta} \sum_{j\neq k\neq i} (1+\lambda\cos\theta_{ijk})^{\zeta} e^{-\eta({R_{ij}}^2+{R_{ik}}^2+{R_{jk}}^2)} f_c(R_{ij}) f_c(R_{ik}) f_c(R_{jk}), \tag{A2}$$

where θ_{ijk} is the angle formed by atoms i, j, and k with atom i at the center. Multiple sets of η, R_s, λ, and ζ are used to define the symmetry function vector for each chemical element [25].

2. Strain perturbation method for pairwise potentials

For the pairwise potential, per-atom energy is expressed as $E_i = \frac{1}{2}\sum_{j:j\neq i} U(r_{ij})$. Subsequently,

$$\pi_i^{\alpha\beta} = \frac{1}{\Omega_i}\frac{\partial E_i}{\partial \epsilon_i^{\alpha\beta}} = \frac{1}{2\Omega_i}\sum_{j:j\neq i}\frac{\partial U(r_{ij})}{\partial r_{ij}^{\alpha}} r_{ij}^{\beta} = \frac{1}{2\Omega_i}\sum_{j:j\neq i} f_{ij}^{\alpha} r_{ij}^{\beta}. \tag{A3}$$

The pairwise form of the atomic virial stress is recovered.

3. Thermodynamic pressure and the global stress tensor

The thermodynamic expression for the pressure is derived from the relation between the pressure P, the Helmholtz free energy F, and the volume V [39]:

$$P = -\left(\frac{\partial F}{\partial V}\right)_{N,T} = k_B T \frac{\partial \ln Q_{N,T}(V)}{\partial V} \tag{A4}$$

where k_B is the Boltzmann's constant, T is temperature, N is the total number of particles, and Q_{NVT} is the partition function for the canonical ensemble:

$$\begin{aligned} Q_{NVT} &= \frac{1}{h^{3N}N!}\iint e^{-\frac{H\left(\boldsymbol{r}^N,\boldsymbol{p}^N\right)}{k_B T}} d\boldsymbol{r}^N d\boldsymbol{p}^N \\ &= \frac{1}{h^{3N}N!}\int e^{-\frac{K\left(\boldsymbol{p}^N\right)}{k_B T}} d\boldsymbol{p}^N \int e^{-\frac{U\left(\boldsymbol{r}^N\right)}{k_B T}} d\boldsymbol{r}^N \end{aligned} \tag{A5}$$

where h is Planck's constant. The integration extends over the coordinates $\boldsymbol{r}^N$ and momenta $\boldsymbol{p}^N$ of all particles, and $H(\boldsymbol{r}^N, \boldsymbol{p}^N)$ is the Hamiltonian of the system, expressed as the sum of the kinetic energy $K(\boldsymbol{p}^N)$ and potential energy $U(\boldsymbol{r}^N)$ arising from interactions among atoms. By transforming the coordinates $\boldsymbol{r}^N$ into dimensionless form $\boldsymbol{s}^N$ and applying the Leibniz integral rule, the pressure can be derived into two parts:

$$\begin{aligned} P &= \frac{k_B T}{Q_{NVT}}\left(\frac{\partial\left(\frac{V^N}{h^{3N}N!}\int e^{-\frac{K\left(\boldsymbol{p}^N\right)}{k_B T}} d\boldsymbol{p}^N \int e^{-\frac{U\left(\boldsymbol{s}^N\right)}{k_B T}} d\boldsymbol{s}^N\right)}{\partial V}\right) \\ &= \frac{k_B T}{V^N}\frac{\partial V^N}{\partial V} + \frac{-1}{\int e^{-\frac{U\left(\boldsymbol{s}^N\right)}{k_B T}} d\boldsymbol{s}^N}\left(\int \frac{\partial U}{\partial V} e^{-\frac{U\left(\boldsymbol{s}^N\right)}{k_B T}} d\boldsymbol{s}^N\right) \end{aligned}$$

$$= \rho k_B T - \left\langle \frac{\partial U}{\partial V} \right\rangle \tag{A6}$$

where ρ is the number density of particles, $\rho k_B T$ is the ideal-gas contribution, and $\langle \frac{\partial U}{\partial V} \rangle$ is the ensemble average of the interatomic potential contribution, i.e., $\frac{\partial U}{\partial V}$ is the static part of global stress.

Letting Ω_C in Eq. (8) include all atoms in the system, we have

$$\pi^{\alpha\beta} = \sum_{i \in \Omega_C} \frac{1}{\Omega_C} \frac{\Delta E_i}{\Delta \epsilon^{\alpha\beta}} = \frac{1}{V} \frac{\Delta U}{\Delta \epsilon^{\alpha\beta}} = \frac{\Delta U}{\Delta V^{\alpha\beta}} . \tag{A7}$$

The static part of global stress in Eq. (A6) is recovered.

[1] J. G. Kirkwood, The statistical mechanical theory of transport processes I. General theory, J. Chem. Phys. **14**, 180 (1946).

[2] E. T. Seppälä, J. Belak, and R. E. Rudd, Effect of stress triaxiality on void growth in dynamic fracture of metals: A molecular dynamics study, Phys. Rev. B **69**, 134101 (2004).

[3] Y. P. Chen, S. Shabanov, and D. L. McDowell, Concurrent atomistic-continuum modeling of crystalline materials, J. Appl. Phys. **126**, 101101 (2019).

[4] J. M. Johnson, H. L. Huang, M. G. Wang, S. Mu, J. B. Varley, A. F. M. A. U. Bhuiyan, Z. X. Feng, N. K. Kalarickal, S. Rajan, H. P. Zhao, C. G. Van de Walle, and J. Hwang, Atomic scale investigation of aluminum incorporation, defects, and phase stability in β-$(Al_xGa_{1-x})_2O_3$ films, APL Mater. **9**, 051103 (2021).

[5] A. C. Li, B. Y. Li, R. E. Rudd, and M. A. Meyers, Dislocation generation in diamond under extreme loading, Matter **6**, 3040 (2023).

[6] K. H. Shi, E. R. Smith, E. E. Santiso, and K. E. Gubbins, A perspective on the microscopic pressure (stress) tensor: History, current understanding, and future challenges, J. Chem. Phys. **158**, 040901 (2023).

[7] W. P. Wu and Z. Z. Yao, Molecular dynamics simulation of stress distribution and microstructure evolution ahead of a growing crack in single crystal nickel, Theor. Appl. Fract. Mech. **62**, 67 (2012).

[8] T. Frolov, Q. Zhu, T. Oppelstrup, J. Marian, and R. E. Rudd, Structures and transitions in bcc tungsten grain boundaries and their role in the absorption of point defects, Acta Mater. **159**, 123 (2018).

[9] Y. Cui and H. B. Chew, Machine-learning prediction of atomistic stress along grain boundaries, Acta Mater. **222**, 117387 (2022).

[10] S. Y. Yuan, A. Y. Liang, C. Liu, A. Nakano, K. Nomura, and P. S. Branicio, Uncovering metallic glasses hidden vacancy-like motifs using machine learning, Mater Design **233**, 112185 (2023).

[11] J. H. Irving and J. G. Kirkwood, The statistical mechanical theory of transport processes. IV. The equations of hydrodynamics, J. Chem. Phys. **18**, 817 (1950).

[12] D. H. Tsai, The virial theorem and stress calculation in molecular dynamics, J. Chem. Phys. **70**, 1375 (1979).

[13] B. D. Todd, D. J. Evans, and P. J. Daivis, Pressure tensor for inhomogeneous fluids, Phys. Rev. E **52**, 1627 (1995).

[14] Z. S. Basinski, M. S. Duesbery, and R. Taylor, Influence of shear stress on screw dislocations in a model sodium lattice, Can. J. Phys. **49**, 2160 (1971).

[15] G. Hummer, N. Gronbech-Jensen, and M. Neumann, Pressure calculation in polar and charged systems using Ewald summation: Results for the extended simple point charge model of water, J. Chem. Phys. **109**, 2791 (1998).

[16] J. Cormier, J. M. Rickman, and T. J. Delph, Stress calculation in atomistic simulations of perfect and imperfect solids, J. Appl. Phys. **89**, 99 (2001).

[17] P. H. Hünenberger, Calculation of the group-based pressure in molecular simulations. I. A general formulation including Ewald and particle-particle–particle-mesh electrostatics, J. Chem. Phys. **116**, 6880 (2002).

[18] A. P. Thompson, S. J. Plimpton, and W. Mattson, General formulation of pressure and stress tensor for arbitrary many-body interaction potentials under periodic boundary conditions, J. Chem. Phys. **131**, 154107 (2009).

[19] Y. P. Chen and A. Diaz, Physical foundation and consistent formulation of atomic-level fluxes in transport processes, Phys. Rev. E **98**, 052113 (2018).

[20] N. C. Admal and E. B. Tadmor, A unified interpretation of stress in molecular systems, J. Elasticity **100**, 63 (2010).

[21] A. Torres-Sánchez, J. M. Vanegas, and M. Arroyo, Examining the mechanical equilibrium of microscopic stresses in molecular simulations, Phys. Rev. Lett. **114**, 258102 (2015).

[22] A. Torres-Sánchez, J. M. Vanegas, and M. Arroyo, Geometric derivation of the microscopic stress: A covariant central force decomposition, J. Mech. Phys. Solids **93**, 224 (2016).

[23] A. P. Thompson, L. P. Swiler, C. R. Trott, S. M. Foiles, and G. J. Tucker, Spectral neighbor analysis method for automated generation of quantum-accurate interatomic potentials, J. Comput. Phys. **285**, 316 (2015).

[24] J. Behler and M. Parrinello, Generalized neural-network representation of high-dimensional potential-energy surfaces, Phys. Rev. Lett. **98**, 146401 (2007).

[25] J. Behler, Atom-centered symmetry functions for constructing high-dimensional neural network potentials, J. Chem. Phys. **134**, 074106 (2011).

[26] J. Behler, Four generations of high-dimensional neural network potentials, Chem. Rev. **121**, 10037 (2021).

[27] See Supplemental Material at http://link.aps.org/supplemental/10.1103/jg6w-fdl8 for (S1) conventional atomic stress calculation methods, (S2) an implementation recommendation for the SP method, (S3) details of MD simulations and relevant calculations, and (S4) practice of the SP method in equilibrium and non-equilibrium MD simulations. The Supplemental Material also contains Refs. [6,20–23,28,29,32,34,35,37].

[28] D. Surblys, H. Matsubara, G. Kikugawa, and T. Ohara, Application of atomic stress to compute heat flux via molecular dynamics for systems with many-body interactions, Phys. Rev. E **99**, 051301 (2019).

[29] D. Surblys, H. Matsubara, G. Kikugawa, and T. Ohara, Methodology and meaning of computing heat flux via atomic stress in

systems with constraint dynamics, J. Appl. Phys. **130**, 215104 (2021).

[30] P. S. Branicio and D. J. Srolovitz, Local stress calculation in simulations of multicomponent systems, J. Comput. Phys. **228**, 8467 (2009).

[31] A. P. Thompson, H. M. Aktulga, R. Berger, D. S. Bolintineanu, W. M. Brown, P. S. Crozier, P. J. I. Veld, A. Kohlmeyer, S. G. Moore, T. D. Nguyen, R. Shan, M. J. Stevens, J. Tranchida, C. Trott, and S. J. Plimpton, LAMMPS—A flexible simulation tool for particle-based materials modeling at the atomic, meso, and continuum scales, Comput. Phys. Commun. **271**, 108171 (2022).

[32] M. Gerstein, J. Tsai, and M. Levitt, The volume of atoms on the protein surface: Calculated from simulation, using voronoi polyhedra, J. Mol. Biol. **249**, 955 (1995).

[33] L. A. Girifalco and V. G. Weizer, Application of the morse potential function to cubic metals, Phys. Rev. **114**, 687 (1959).

[34] A. Stukowski, Visualization and analysis of atomistic simulation data with OVITO—The open visualization tool, Modell. Simul. Mater. Sci. Eng. **18**, 015012 (2010).

[35] J. A. Hauch, D. Holland, M. P. Marder, and H. L. Swinney, Dynamic fracture in single crystal silicon, Phys. Rev. Lett. **82**, 3823 (1999).

[36] E. B. Tadmor, R. S. Elliott, J. P. Sethna, R. E. Miller, and C. A. Becker, The potential of atomistic simulations and the knowledgebase of interatomic models, Jom-Us **63**, 17 (2011).

[37] K. Kim, A. Dive, A. Grieder, N. Adelstein, S. Kang, L. F. Wan, and B. C. Wood, Flexible machine-learning interatomic potential for simulating structural disordering behavior of $Li_7La_3Zr_2O_{12}$ solid electrolytes, J. Chem. Phys. **156**, 221101 (2022).

[38] https://github.com/SuyueYuan/strain_perturbation_atomic_virial_stress.

[39] H. B. Callen, *Thermodynamics and an Introduction to Thermostatistics*, 2nd ed. (Wiley, New York, 1993).